ON THE STRUCTURE AND PROPERTIES OF ALLOY B-1950

B. H. Kear and D. E. Fornwalt

Pratt & Whitney Aircraft Middletown, Conn. 06457

#### ABSTRACT

The microstructure of B-1950 consists of dendrites of cooling  $\gamma'$  in  $\gamma$ , interspersed with  $\gamma/\gamma'$  eutectic and particles of  $M_3B_2$ . Ageing at temperatures in the range  $1600^{\circ}-2100^{\circ}F$  causes precipitation of a new boride phase at the expense of  $M_3B_2$ . The new phase has a tetragonal structure ( $a_0=7.99$ , Co=10.72), with an approximate composition  $W_0.5Cr_0.5B_12C_0.3$ , corresponding with an  $MB_{12}$ -type boride (space group P42/nnm). Particles of this phase precipitate preferentially along the borders of the dendrites, and the larger particles ( $\geq 200\mathring{A}$  in size) have a characteristic square-based dipyramidal morphology. Three principal variants, each with two sub-variants, of the  $MB_{12}$  phase have been identified by TEM, with the c-axis of each variant parallel to a cube axis in the  $\gamma/\gamma'$  matrix.

The distribution of  $\gamma/\gamma'$  eutectic in B-1950 is similar to that of Hf-doped Mar-M200. The improved creep rupture properties in these materials, compared with Mar-M200, is attributed to slip dispersal by the massive  $\gamma'$  particles in the  $\gamma/\gamma'$  eutectic decorating the grain boundaries, and the effect this has on inhibiting crack initiation and possibly crack growth in creep. It is proposed that a uniform distribution of extremely fine particles of the MB12 phase would make a useful contribution to the creep strength of B-1950 at intermediate temperatures.

## Introduction

Starting with the pioneering work of Decker and Freeman, (1) much effort in the superalloy field has been devoted to determining the influence on creep properties of trace amounts of certain beneficial additives, e.g. B, C and Zr. It is now known that in a given alloy system, optimum creep properties frequently correlate with a certain critical combination of these elements. The earlier work focussed on total B + Zr content and B/Zr ratio for a fixed C content. More recently, the emphasis has shifted towards the consideration of total B + C content and B/C ratio. (2-4) It now seems clear that a high B/C ratio consistently gives improved creep rupture properties in many alloy systems. Maxwell et al (4) have exploited this discovery in the development of a new series of commercial alloys. Alloy B-1950\*, which is essentially a high B/C ratio modification of Mar-M200, is one of the new alloys in this series. Current interest in B-1950 as a potentially useful alloy prompted the present investigation.

# Microstructure

In the as-cast condition, the alloy was composed of dendrites of cooling  $\gamma'$  in  $\gamma$ , interspersed with an essentially continuous network of about 10 vol. pct.  $\gamma/\gamma'$  eutectic, and a few large, irregularly-shaped particles of  $M_3B_2$ , Fig. 1. By electron microprobe analysis, it was established that the dendrites were rich in W and Cr, whereas the interdendritic regions were rich in Ti, Al and Nb. The W-rich  $M_3B_2$  boride phase (tetragonal structure, with  $a_0 = 5.70$ , Co = 3.10) contained Cr and minor amounts of Nb and C.

Compared with Mar-M200, the microstructure of B-1950 contains a somewhat larger volume fraction of  $\gamma/\gamma'$  eutectic, and particles of M3B2 rather than MC. The larger amount of eutectic in B-1950 can be rationalized in terms of changes in the interdendritic composition due to the formation of W, Cr-rich M3B2 rather than Ti, Nb-rich MC. Thus, the fact that there is insufficient carbon in B-1950 to give MC must mean that more Ti and Nb become available to form  $\gamma'$  phase. Again, taking W and Cr out of solution during precipitation of the M3B2 phase should increase the propensity for  $\gamma'$  formation, since these elements tend to stabilize the  $\gamma$  phase.

Detectable changes in the general microstructure due to heat treatment (e.g. 1975°F/4 hrs. + 1650°F/10 hrs.) were observed only when the material was examined after electro-etching using a solution of 10% HCl in methanol. In this condition, the borders of the dendrites were seen to be decorated with clusters of fine particles, Figs. 2 and 3. Moreover, many of the dendrites contained one or more sets of intersecting bands, Fig. 2. Surface trace analysis of these crystallographic bands showed that they were traces of {111} planes, indicating preferential precipitation on slip bands in the material. It is noteworthy that the precipitate decorated slip bands were located only within the confines of the dendrites, and did not extend into the  $\gamma/\gamma^*$  eutectic regions.

Ion microprobe analysis of the heat treated material gave a clear picture of the distribution of boron in the alloy. The dendrite cores were found to be deficient in boron, whereas the dendrite borders were enriched in boron, Fig. 4(b). Significant enrichment of boron in the interdendritic regions correlated with the presence of massive  $M_3B_2$  particles. Some enrichment of the dendrite borders in W, and to a lesser extent in Cr, was also noted, Figs. 4(c) and (d). These observations, taken together with Figs. 2 and 3, may be taken as strong evidence that the finely divided particles decorating the dendrite borders are W, Cr-rich borides.

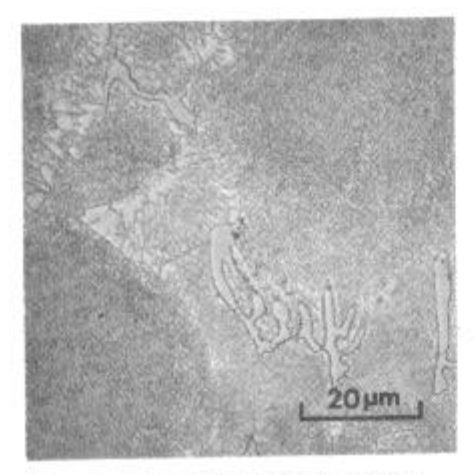
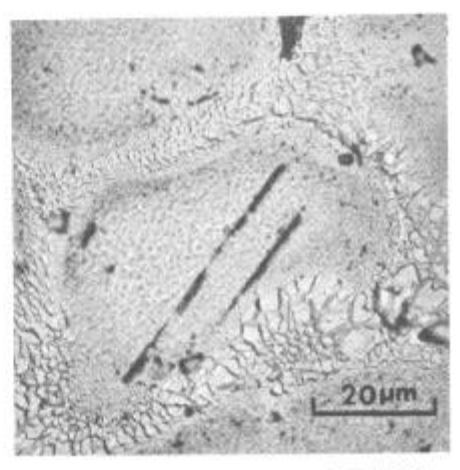


Fig. 1 Microstructure of E-1950.



Pig. 2 Microstructure of B-1950 after electro-etching, showing distribution of boride phases.

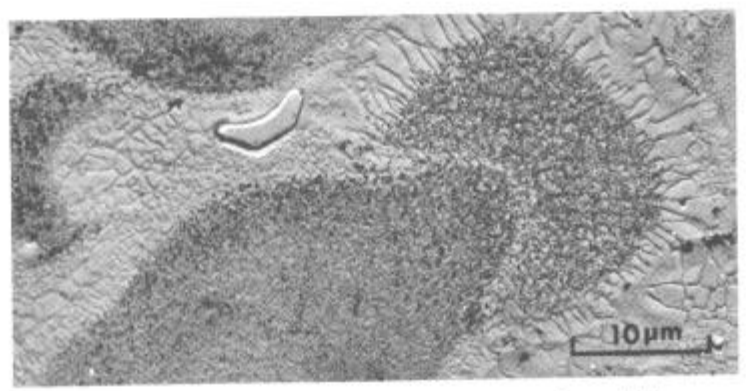


Fig. 3 Extraction replica, showing concentration of fine particles of MB<sub>12</sub> phase along the borders of the dendrites.

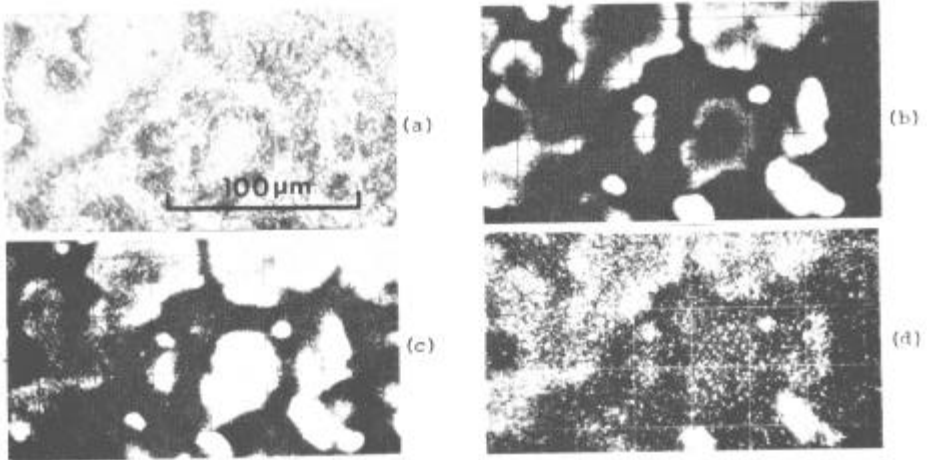


Fig. 4 Ion microprobe analysis of R-1950; (a) light micrograph, (b) R-ion image, (c) Cr-ion image and (d) M-ion image.

# Diffraction Analysis

X-ray diffraction analysis was performed on extracted residues obtained by selective dissolution of the  $\gamma+\gamma'$  matrix. The fine particles of the boride phase were separated from the very coarse  $^{\rm M}_3{\rm B}_2$  particles by a sedimentation technique. Electron diffraction analysis was carried out on extracted replicas and on thin foils of the material prepared by an established procedure. The X-ray diffraction data obtained from the fine boride particles is presented in Table I. The pattern was indexed on the basis of a tetragonal cell, with  $a_0=7.99$ , Co = 10.72 and c/a = 1.34. A comparison of the systematic non-extinctions of the observed reflections with those published in the International Tables for X-ray Crystallography indicated a structure belonging to space group P42/nnm. Chemical analysis of a small quantity of the extracted phase gave an approximation composition of  $W_{0.5}{\rm Cr}_{0.5}{\rm Bl}_2{\rm C}_{0.3}$ . The new boride phase, therefore, was designated  ${\rm ^{MB}_{12}}$ .

Measurements made on polycrystalline electron diffraction patterns obtained from clusters of fine MB12 boride particles supported on extraction replicas, e.g. as in Fig. 3, gave interplanar spacings consistent with those obtained by X-ray diffraction. Analysis of single crystal electron diffraction patterns obtained from isolated particles and decorated slip bands in thin foils also gave consistent results. Electron diffraction analysis was used also to determine the orientation relationships between matrix and precipitate. (5) As shown in Fig. 5(a), a preferred orientation for the MB12 phase evidently exists, since particles of similar shape (square, or rhombus-shaped for the larger particles) assume the same orientation in the thin foil. These two different shapes represent projections of particles with an actual shape that can best be described as a square-based dipyramid. Smaller particles tend to have more rounded morphologies. Using the dark field imaging technique, three principal variants of the MB12 phase were detected, with the c-axis (i.e. long axis of dipyramid) of each variant parallel to a <100> axis in the matrix. Furthermore, each principal variant possessed two sub-variants corresponding with two equivalent orientations obtained by rotation of a principal variant about its c-axis. These orientation relationships were best seen in a [001] matrix orientation foil, Fig. 6, where the two sub-variants of the principal variant lying parallel to [001] showed up in projection as two differently oriented squares, Figs. 6(c) and (d). In this same orientation foil, it was not possible to distinguish between the two sub-variants of each principal variant parallel to [010] and [100] matrix directions, since each pair was imaged simultaneously in dark field with the same reflection, e.g. 002 and  $00\overline{2}$  in Figs. 6(e) and (f). Other orientation foils were indexed in a similar manner, and the different variants were imaged systematically using the appropriate reflections.

### Phase Transformations

Ageing at temperatures in the range  $1600^{\circ}-2000^{\circ}F$  caused precipitation of MB12, apparently at the expense of M3B2, Table II. This transformation was essentially complete after ageing at  $1975^{\circ}F$  for 100 hours. It appears that the boron given up by the M3B2 phase diffuses away from the  $\gamma/\gamma$  eutectic zone into the outer edges of the dendrites where it reacts with W and Cr to form the MB12 phase. In the low temperature range,  $\leq 1600^{\circ}F$ , precipitation of MB12 was accompanied by precipitation of coherent  $\gamma$  phase within the massive  $\gamma'$  particles characteristic of the  $\gamma/\gamma'$  eutectic constituent, Fig. 7. This phenomenon has been reported previously for a variety of superalloys, and is apparently a manifestation of retrograde solubulity of  $\gamma$  in  $\gamma'$ . (6) Ageing at temperatures in the range  $2200-2250^{\circ}F$  resulted in a gradual transformation of MB12 into the more W, Cr-rich M5B3 phase. Above the incipient melting point of the alloy, the stable boride phase was M3B2.

Under all conditions of ageing favorable to the precipitation of MB $_{12}$ , the precipitate invariably occurred in a finely divided form along the borders of the dendrites. Moreover, within the precipitation zone, the size of the

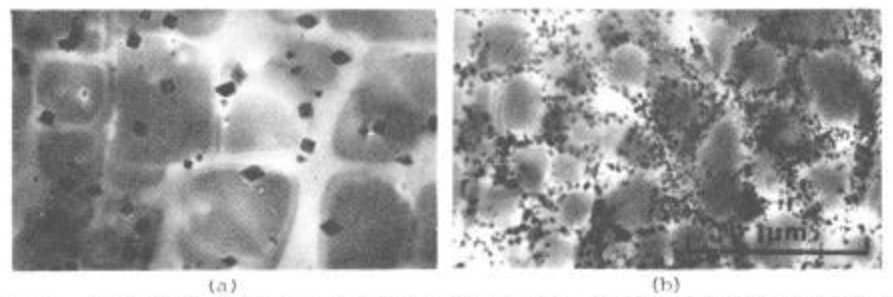


Fig. 5 Thin foil micrographs of the  $^{48}17$  phase showing (a) dipyramidal morphology, and (b) concentration at  $\gamma/\gamma$  interfaces. Specimen aged at 1850°F for 200 hours.

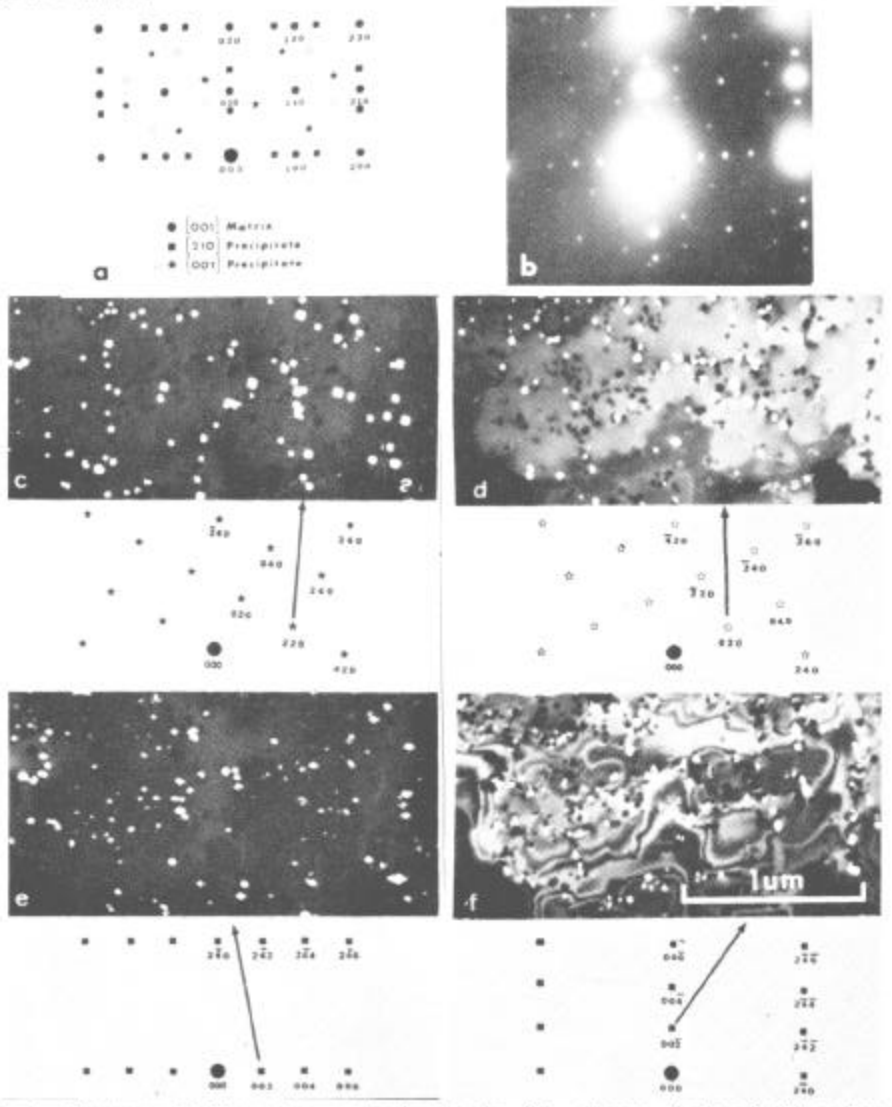


Fig. 6 Electron diffraction analysis of the MB $_{12}$  phase; (a) and (b) schematic and actual diffraction patterns in an [991] matrix orientation, (c) - (f) dark field images of the precipitate using the indicated reflections. Specimen aged at  $1850^{\circ}\text{P}/100$  hours.

particles clearly was dependent on position within the zone. Thus, the edges of the precipitation zone invariably contained fewer and larger particles than was characteristic of the middle of the zone, Fig. 5. Comparing the effects of different heat treatments, a predictable increase in particle size with ageing time and temperature was observed, but the particle coarsening was not as pronounced as might be expected in view of the high diffusivity of boron at high temperatures. Thus, as shown in Fig. 8, even after ageing at 2000°F for 100 hours, the average particle size is only ~1000Å, which is small compared with the  $\gamma^{\prime}$  particle size. Slow coarsening rates for the MB $_{12}$  phase can be understood if the matrix solubility for boron is very low. Although not shown in Fig. 8, evidence for precipitation of MB12 in small amounts was first detected in material aged at 1600°F for 20 hours. After this heat treatment, the particles ranged in size from 25-200Å. In all cases, the  ${\rm MB}_{12}$  boride particles appeared to be concentrated in the  $\gamma$  matrix or at the  $\gamma/\gamma^{-1}$  interfaces. This seems reasonable because the W and Cr required to form the boride phase tend to be concentrated in the \gamma phase.

### Discussion

Table III compares the average creep rupture properties of Mar-M200, B-1950 and Mar-M200 + 2% Hf, all in the conventionally cast, polycrystalline condition. It can be seen that the relatively minor modifications to the composition of Mar-M200 impart a substantial improvement in rupture life, without sacrificing rupture ductility. It is pertinent to speculate here on why such small compositional changes can exert such a profound influence on creep properties.

Previous studies(7,8) have described the significant microstructure/property relationships that are characteristic of Hf-doped Mar-M200. The principal findings of these studies will be summarized. Alloying Mar-M200 with 1-3 wt. pct. Hf has the effect of increasing the volume fraction of  $\gamma/\gamma$  eutectic, particularly along grain boundaries, where a more or less continuous film of eutectic is developed. This is due to segregation of Hf to the interdendritic/grain boundary regions, and its incorporation into the  $\gamma/\gamma'$  eutectic constituent. At intermediate temperatures, Hf-rich  $\gamma'$  phase is stronger than the normal  $\gamma+\gamma'$  superalloy microstructure. Moreover, as is typical of all single phase  $\gamma'$  alloys, Hf-rich  $\gamma^*$  exhibits an extremely fine, homogeneous slip structure, in sharp contrast to the very coarse, heterogeneous slip structure typical of Y+Y' superalloys. Thus, the presence of massive Hf-rich  $\gamma'$  in the  $\gamma/\gamma'$  eutectic lining the grain boundaries can serve to blunt slip bands and prevent the build up of stress concentrations in the grain boundaries. The improvement in the creep rupture properties at intermediate temperatures, therefore, has been ascribed to the presence of strong, ductile Hf-rich Y' phase along the grain boundaries, which reduces the potential for grain boundary cavitation and cracking, and possibly crack growth, by efficient slip dispersal. Other effects, such as the formation of a more favorable distribution of grain boundary  $M_{23}C_6$ carbide, and possible scavenging of deleterious tramp elements, such as sulphur, (8) may also contribute to the improvement in properties, but these are probably not as critical as the distribution of  $\gamma/\gamma'$  eutectic. The present work has shown that the distribution of  $\gamma/\gamma$ ' eutectic in B-1950 is similar to that of Hf-doped Mar-M200. It is natural, therefore, to attribute the improved properties to the same cause; namely, dispersal of slip by massive  $\gamma^{\star}$  particles in the  $\gamma/\gamma'$  eutectic lining the grain boundaries, and the effect this has on inhibiting crack initiation, and possibly crack growth in creep. Evidence for slip dispersal in B-1950 lightly deformed at ambient temperatures is shown in Fig. 9. In the  $\gamma+\gamma'$  dendrites, the slip bands are sharply defined, i.e coarse slip, whereas in the  $\gamma/\gamma'$  eutectic regions they are more diffuse in character, i.e. fine slip.

Evidence that heterogeneous slip bands intersecting grain boundaries in Nimonic 80A can give rise to premature cavitation in creep has been obtained by Dyson.  $^{(9,10)}$  Using the high voltage electron microscope, he found that the grain boundaries in this material became decorated with submicron size cavities

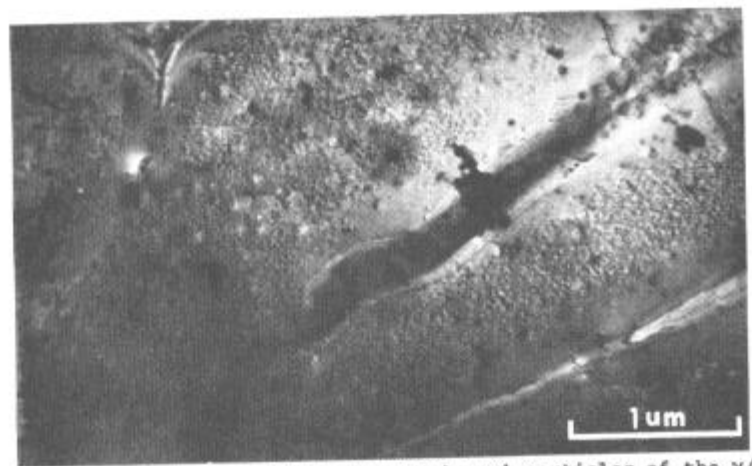


Fig. 7 Precipitation of  $\gamma$  within the massive  $\gamma$ ' particles of the  $\gamma/\gamma$ ' eutectic. Note precipitate free zones where thin ribs of  $\gamma$  phase separate the massive  $\gamma$ ' particles. Specimen aged at 1400°F/300 hours.

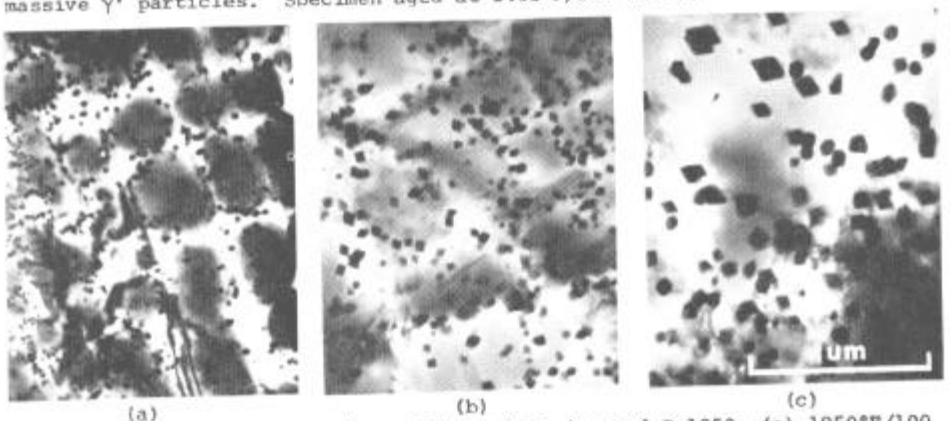


Fig. 8 Illustrating coarsening of MB<sub>12</sub> phase in aged B-1950; (a) 1850°F/100 hours, (b) 2000°F/100 hours, and (c) 2100°F/100 hours.

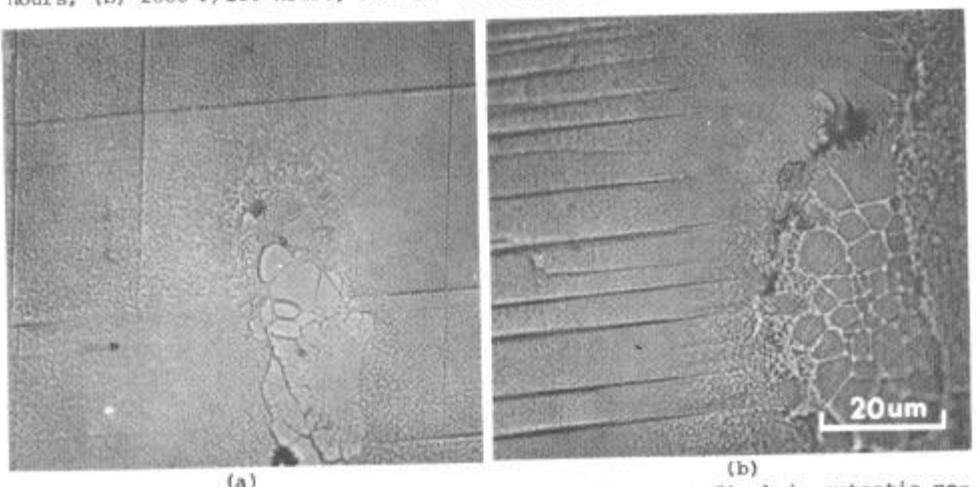


Fig. 9 Illustrating changes in slip character (coarse + fine) in eutectic regions; (a) eutectic within a grain, (b) eutectic at a grain boundary.

after a pre-strain followed by a short heat treatment. The cavities are located along the lines of intersections of slip bands with the grain boundaries. The majority of the cavities grow on boundaries having an orientation nearly parallel to the maximum tensile stress axis, apparently because of the presence of a residual tensile stress across the boundaries. Despite this, when the material is subjected to a creep deformation, the relatively few submicron cavities formed by the prior deformation on the transverse boundaries grow into larger cavities that link up to form cracks, and eventually give rise to creep fracture. This, of course, is consistent with the usual finding that creep cavitation occurs in boundaries that are transverse to the maximum principal stress axis. Clearly, the present model predicts that both Hf-doped Mar-M200 and B-1950 would be less cavitation prone than Mar-M200, and experiments are being conducted to determine if this is, indeed, the case.

Grain boundary cavitation due to heterogeneous slip may also explain the striking differences in castability of these alloys. Experience has shown that in the casting of shrouded parts, transverse grain boundary cracking cannot be avoided in Mar-M200. On the other hand, such cracking is seldom observed in Hf-doped Mar-M200 and in B-1950. In view of the preceding discussion, it seems reasonable to ascribe the improved castability of these alloys to the presence of  $\gamma/\gamma^{\prime}$  eutectic at the grain boundaries, which should prevent cavitation and cracking by the Dyson mechanism. Evidence for pre-strain in a shrouded part of B-1950 is shown in Fig. 2. In this case, the cooling rate from the melt apparently was slow enough to permit decoration of the slip bands with MB12.

Table III shows that the creep strengths of B-1950 and Hf-doped Mar-M200 are comparable, despite the fact that B-1950 contains a fine distribution of a second hardening phase; namely, MB12. Examination of thin foils indicated that the reason for this is that a low volume fraction of fine precipitates on the scale observed does not appear particularly effective in impeding dislocation motion in creep; apparently, the dislocations can easily circumvent the particles by cross slip or climb. Thus, as shown in Fig. 10, in 1800°F creep, the average dislocation density seems to be independent of the distribution of the MB<sub>12</sub> phase. This would not have been the case if the MB<sub>12</sub> phase had been effective in dislocation pinning; on the contrary, the dislocations would have concentrated in these regions. In 1400°F creep, the actual state of affairs was more difficult to interpret owing to the higher overall dislocation density. However, it did appear from the observed uniform distribution of stacking faults that slip activity was similar in all areas of the thin foil, including regions of high concentrations of MB12 phase, Fig. 11. It should perhaps be noted that it is well known that the deformation mode in Mar-M200 at intermediate temperatures (~1400°F) involves shearing of γ' particles by a/3. <112> dislocations (connected to stacking faults), either singly or in pairs, whereas at high temperatures (~1800°F) shearing of  $\gamma'$  particles occurs by diffusive slip of pairs of a/2 <110> dislocations coupled together by antiphase boundary. (11) This explains the appearance in B-1950 of stacking faults at 1400°F, and no faults at 1800°F.

Anomalously high values for the activation energy for creep, corresponding with low steady state creep rates, have been found in alloys containing a uniform distribution of extremely fine pre-precipitates (< 30A dia.). (12) This suggests that the MB12 phase might be useful for creep strengthening if conditions could be devised to obtain a uniform distribution of particles on a fine enough scale, while maintaining the favorable distribution of  $\gamma^{*}$  in  $\gamma$ . Possibly, this could be done via powder metallurgy processing.

TABLE I X-RAY DIFFRACTION DATA FOR THE MB12 PHASE

d <sub>meas</sub>	$\frac{d_{calc}}{d_{calc}}$	<u>hkl</u>	<u>I/I</u> o
5.36	5.36	002	15
3.998	3.998	200	15
3.212	3.204	922	15
2.821	2.824	220	40
2.681	2.681	004	50
2.454	2.459	131	70
2.226	2.226	024	20
2.064	2.064	133	100
1.944	1.945	224	30
1.786	1.787	006	50
1.635	1.635	135	5
1.483	1.487	244	5
1.389	1.391	236	5
1,360	1.360	351	15
1.332	1.332	600 046	10
1.314	1.314	146	30
1.282	1.282	345	30
1.265	1.265	155	20
1.240	1.240	451	5
1.195	1.193	064	20
1.076	1.077	272	20
1.024	1.024	464	20

Tetragonal:  $a_0 = 7.99$ ,  $C_0 = 10.72$ , c/a = 1.342

TABLE II
PHASES OBSERVED BY X-RAY DIFFRACTION

Heat Treatment		Phases Observed	
Temp., °F	Time, Hours	M3B2	W0.5Cr0.5B12
As Received		Major	N.D.*
1400	100	Major	N.D.
1600	100	Major	N.D.
1850	20	Major	Trace
1850	100	Major	Medium
1850	200	Medium	Medium
1925	100	Trace	Major
2000	100	N.D.	Major
2100	100	N.D.	Major

\*Not Detected

AVERAGE CREEP RUPTURE PROPERTIES OF CONVENTIONALLY CAST B-1950 AND OTHER NICKEL-BASE SUPERALLOYS

Test Conditions	Alloy Designation	Rupture Life (Hours)	Rupture Elongation (%)
	B-1950*	460	3
1400°F/94 ksi	Mar-M200	<10	2
	Mar-M200 + 2% Hf	360	3
	B-1950*	115	5
1800°F/29 ksi	Mar-M200	60	4
	Mar-M200 + 2% Hf	80	5
*Data from Bof	(4)		

\*Data from Ref. (4).

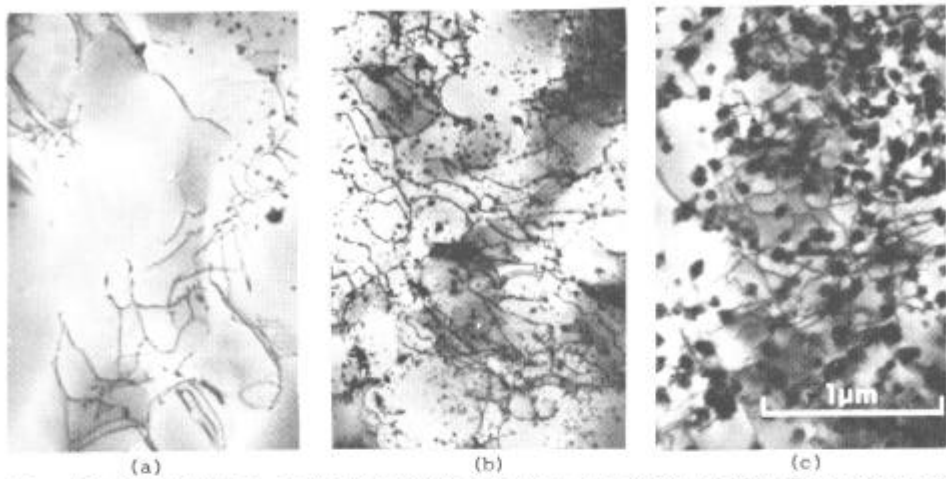


Fig. 10 Distribution of dislocations and MB12 phase in B-1950 after creep at 1800°F/29 ksi for 100 hours. Note dislocation/precipitate interactions in (b)

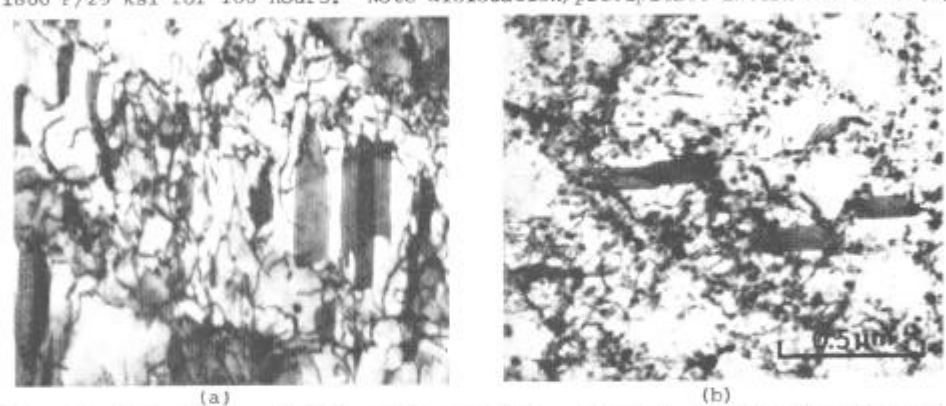


Fig. 11 Distribution of dislocations and  $MB_{12}$  phase in B-1950 after creep at  $1400^{\circ}\text{P}/36$  ksi for 300 hours.

## REFERENCES

- 1. R.F. Decker and J.W. Freeman: Trans. TMS-AIME, 1960, Vol. 218, pp 277-285.
- R. Yoda, et al: High Temperature Strength and Microstructure of Nickel-Base Heat Resisting No. 64C Alloy, Proc. Japan-U.S. Seminar on the Physical Metallurgy of Heat Resisting Alloys, WSF, September 1972.
- F.F. Khimiushin: High Temperature Steels and Alloys, "Metallurgiya" Pub. House, Moscow, 1969; FTD-HC-23-391 Parts I and II, 1971.
- D.H. Maxwell, J.F. Baldwin and J.F. Radavich, Materials Science Symposium, Cincinnati, 1975, paper #56, "A New Concept in Superalloy Ductility".
- D.E. Fornwalt, A.R. Geary and B.H. Kear: Proc. Thirty-Second Annual EMSA Meeting, 1974, p 492.
- J.M. Oblak, J.E. Doherty, A.F. Giamei and B.H. Kear: Met. Trans., 1973, Vol. 5, p 1252.
- J.E. Doherty, B.H. Kear and A.F. Giamei: J. Metals, 1971, Vol. 23, p 59.
- B.H. Kear, A.P. Giamei and J.E. Doherty: Proc. Third Int. Conf. on the Strength of Metals and Alloys, Cambridge, 1973, Vol. 1, p 134.
- 9. B.F. Dyson and D.E. Henn: J. Microscopy, 1973, Vol. 97, p 165.
- 10. B.F. Dyson: Canadian Met. Quart., 1974, Vol. 13, #1, p 237.
- B.H. Kear and J.M. Oblak: J. de Physique, "Dissociation des Dislocations", Beaune, 1976, pp C7-35.
- 12. P.R. Strutt: Physics Bulletin, 1974, Vol. 25, p 341.